



# The Influence of NiO Nanoparticles on Structural, Optical and Dielectric Properties of CMC/PVA/PEDOT:PSS Nanocomposites

E. Salim<sup>1</sup> · A. E. Tarabiah<sup>2</sup>

Received: 30 January 2023 / Accepted: 21 February 2023 / Published online: 7 April 2023  
© The Author(s) 2023

## Abstract

The solution casting process was used to fabricate nanocomposite samples composed of carboxymethylcellulose (CMC), polyvinyl alcohol (PVA), poly(3,4-ethylenedioxythiophene) polystyrene sulfonate (PEDOT:PSS) and filled with varied concentrations of nickel oxide nanoparticles (NiO NPs). The effect of NiO nanoparticles on the structural, optical, and electrical properties of the pure CMC/PVA/PEDOT:PSS mixture was studied and discussed. X-ray diffraction (XRD) and transmission electron microscopy (TEM) analysis revealed that the NiO NPs are cubic in phase and range in size from 10 to 55 nm. The XRD analysis of the incorporated films indicated that the NiO NPs crystallinity increased at expense of the CMC/PVA/PEDOT:PSS composites. Fourier Transform Infrared (FTIR) examination revealed the main absorption vibrational peaks of CMC, PVA, PEDOT:PSS, and Ni-O, whose intensities changed randomly after filling, revealing the intermolecular interaction between the nanocomposite components. The UV and visible range absorption spectra showed a sharp peak around 228 nm for the pure blend, which can be assigned to the  $\pi \rightarrow \pi^*$  transition. After being filled with NiO NPs, the nanocomposites produced displayed new peaks at 292 and 422 nm that steadily increased with increasing NiO NPs concentration. The optical energy gap ( $E_g$ ) was computed, and it was discovered that when the NiO NPs content increased, the  $E_g$  decreased (from 4.88 to 4.06 eV). At room temperature and over a wide frequency range, between  $10^{-1}$  and  $10^7$  Hz, the samples' impedance, AC conductivity, and dielectric qualities were examined. Increased NiO NPs content was seen to gradually enhance dielectric loss (up to 2255), and dielectric constant (up to 311). The AC conductivity of the filled samples is also enhanced and corresponds to Jonscher power law. By analysing impedance components of the  $Z^*$ , the equivalent electrical circuit for each sample was determined. Because of the considerable improvement in optical and electrical properties, these composite films could compete for usage in optoelectronic applications.

**Keywords** CMC · PVA · PEDOT:PSS · NiO-nanoparticles · Dielectric properties · Polymer nanocomposites

## 1 Introduction

Recent decades have seen tremendous technological advancements, as well as an increase in the number of digitized goods and services. Furthermore, “frontier technologies” like artificial intelligence (AI), robots, and nanotechnology seem to have the potential to hasten the rate of development. While nanotechnology has many applications,

three of them—materials science, nanomedicine, and device engineering—are laying the groundwork for our future. Compared to their bulk counterparts, nanomaterials exhibit radically different mechanical, electrical, magnetic, thermal, and optical properties, which have attracted considerable attention. Transition metal oxides, such as nickel oxide (NiO) nanoparticles, have recently received a lot of attention from researchers due to their low cost, stability, and optoelectronic characteristics. NiO is used in electrochemical capacitors, batteries, gas sensors, magnetic materials, and catalysis [1].

Utilizing NiO NPs' advantages through composites made of polymers and/or polymer blends is one of the more alluring short-term strategies. Carboxymethylcellulose (CMC), polyvinyl alcohol (PVA) and poly(3,4-ethylenedioxythiophene) polystyrene sulfonate (PEDOT:PSS) are

✉ E. Salim  
ehabahmed@mans.edu.eg

<sup>1</sup> Physics Department, Faculty of Science, Mansoura University, Mansoura, Egypt

<sup>2</sup> Dental Biomaterials Department, Faculty of Oral and Dental Medicine, Delta University for Science and Technology, Gamassa, Egypt

interesting polymers that can be used significantly in the industry due to their good electrical, optical and mechanical properties. CMC is one of the cellulose derivatives and water-soluble anionic which forms good films and gels at high temperatures [2]. Its structure is composed of hydroxyl (OH) and carboxylate (COO) groups that promote interactions between the various fillers in the polymeric system [3]. Among CMC's unique characteristics are its transparency, high viscosity, biocompatibility, and biodegradability [4]. It is used in a variety of applications, such as paper manufacturing, textile printing, and medication delivery [5].

PVA is a polar semi-crystalline polymer containing OH groups that can cooperate by hydrogen bonding with various fillers in the polymeric systems. PVA has strong dielectric properties, excellent charge storage capacity, and filling-dependent electric, dielectric, and optical characteristics. This has made the PVA an option for the electronics and optoelectronics industries [6, 7]. PEDOT:PSS is a conductive biocompatibility polymer with proper transparency and excessive thermal stability, making it successful in electrostatic coatings, flexible electronics, bioelectronics, and tissue engineering [8].

Recent research has employed the solution casting approach to make lightweight, elastic polymer nanocomposites comprising CMC, PVA, PEDOT:PSS, and NiO NPs with improved electrical characteristics for use in electronics. In this work, a CMC/PVA/PEDOT:PSS mixture has been employed as a host polymeric matrix, and NiO NPs have been used as conducting fillers. In a comprehensive investigation of the structural, optical, and electrical characteristics of this system, many techniques and processes are presented. This research is of crucial academic importance as it helps us understand the fundamental nanoscale mechanisms that enhance the functional properties of composites.

## 2 Experimental Section

### 2.1 Materials

NiO NPs (particle size < 50 nm, 99.8% trace metal basis), PVA (Mw 31,000–50,000 g/mol, 98–99% hydrolyzed), CMC (Mw 250,000 g/mol), and PEDOT:PSS (1.3 wt % dispersion in H<sub>2</sub>O, conductivity 1 S/cm), were all purchased from Sigma-Aldrich. All materials used in this experiment were used as supplied without any further purification.

### 2.2 Preparation of CMC/PVA/PEDOT:PSS/NiO NPs

1 g CMC and 2 g PVA were dissolved separately in 100 ml deionized water at 75 °C and 90 °C respectively, and then blended and stirred (500 rpm) for 3 h after being completely

dissolved. Following that, 20 ml of the dissolved CMC/PVA and 0.6 ml of PEDOT:PSS were mixed in five equal parts and stirred for 1 h. Then, 0, 0.002, 0.004, 0.006, and 0.008 g of NiO NPs dispersed in 1 ml deionized water were incorporated into mixtures and stirred for an additional 1 h. Finally, the mixed solutions were poured into plastic Petri dishes (Diameter = 55 mm) and dried at 50 °C. The prepared films were labeled S0, S1, S2, S3, and S4 based on the amount of NiO NPs incorporated gradually. To avoid any trace moisture, the dried films were placed in a desiccator loaded with silica gel desiccants for further drying.

## 2.3 Characterizations

Fourier transform infrared (FTIR 430-JASCO, Japan) spectrometer data were taken in the 400–4000 cm<sup>-1</sup> range. X-ray diffraction (XRD) patterns of the samples were obtained by DIANO company USA with CuK radiation at the Bragg angle  $2\theta = 5^\circ$  to  $70^\circ$ . Optical absorption of the nanocomposite films was tested using UV–visible spectrophotometer (JASCO V-630-Japan). Transmission electron microscopy (TEM, JEOL/ JEM/1011, Japan) was used to examine the size of NiO NPs. Broadband dielectric spectroscopy (Novo control Turnkey Concept 40 System) was used to measure the impedance and dielectric properties of the films at room temperature (303 K).

## 3 Results and Discussion

### 3.1 XRD and TEM Analysis

Figure 1 shows the XRD patterns of powdered NiO NPs, and both pure and filled CMC/PVA/PEDOT:PSS blend with NiO NPs. The figure demonstrated that, in accordance with JCPDS chart No. 47-1049, the XRD of NiO NPs revealed distinct peaks at  $2\theta = 37.2, 43.3,$  and  $62.9$  that were attributed to planes (111), (200), and (220), respectively. This verifies the creation of the cubic phase of NiO NPs [9, 10]. The NiO nanoparticles' sharp peaks reveal their great crystallinity, and the absence of any additional peaks demonstrates the sample's high purity and absence of impurities [11]. The Scherrer equation is used to compute the NiO nanoparticles' mean crystallite size [12], which is found to be 21 nm. Figure 2a, b show the TEM image and a histogram distribution plot for NiO NPs dispersed in deionized water, which supports the XRD findings that the particles are crystalline, approximately spherical, with a non-uniform dispersion and a mean crystallite size ~ 27 nm.

For the pure CMC/PVA/PEDOT:PSS mixture, the large broad peak at  $2\theta \approx 19.7^\circ$  can be assigned to the semi-crystalline nature of the PVA [13, 14] and the crystalline cellulose

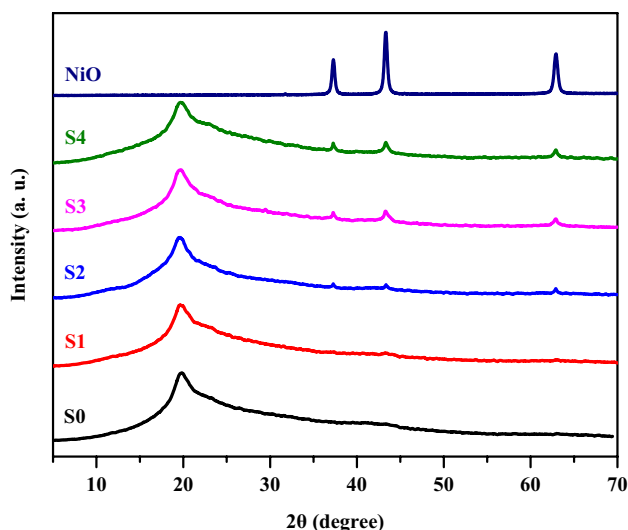


**Fig. 1** XRD patterns of NiO NPs, and CMC/PVA/PEDOT:PSS composites filled with different NiO NPs.

structure of the CMC [15]. The XRD shows that the peak at  $2\theta \approx 19.7^\circ$  has further decreased and that the crystallinity of the nanoparticles grew at the expense of the CMC/PVA/PEDOT:PSS mixture matrix. This enhancement in the blend's amorphous nature is indicative of high ionic diffusivity, which can result in enhanced ionic conductivity [4].

### 3.2 FTIR Analysis

Figure 3 shows the FTIR spectra for CMC/PVA/PEDOT:PSS composite filled with different NiO NPs content. The functional groups produced in the prepared samples manifested

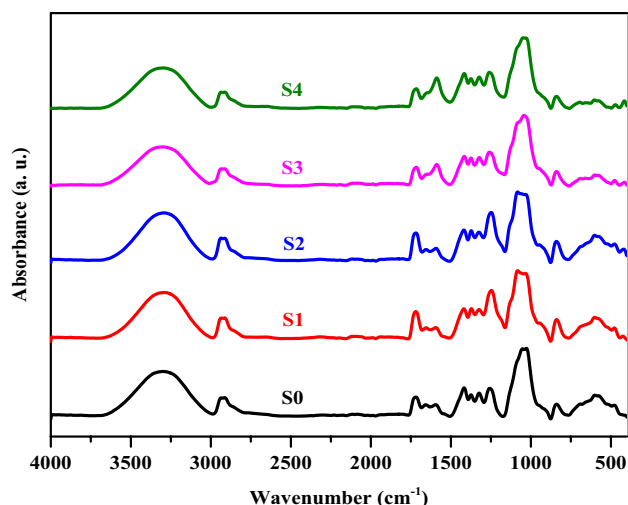


**Fig. 3** FTIR spectra of CMC/PVA/PEDOT:PSS composites filled with different NiO NPs.

in the spectra as distinctive bands of bending and stretching vibrations.

The spectra of the pure blend show the characteristic absorption bands of PVA at 1373, 1256, and 863  $\text{cm}^{-1}$  as a result of CH<sub>2</sub> bending vibration, 2907  $\text{cm}^{-1}$  due to CH<sub>2</sub> symmetrical stretching, and 1086  $\text{cm}^{-1}$  due to CO stretching [16–19]. The CMC characteristic peaks were also observed at 1603  $\text{cm}^{-1}$  due to asymmetric COO stretching, and 1419  $\text{cm}^{-1}$  due to CH<sub>2</sub> scissoring [17]. Furthermore, the PEDOT:PSS has bands at 1656  $\text{cm}^{-1}$  due to C=C stretching and 3307  $\text{cm}^{-1}$  due to OH stretching [20]. Table 1 lists additional band designations for the FTIR spectra of the synthesized samples. After being filled with NiO NPs, the majority of these absorptions became less intense. Moreover, a new peak, characterized as Ni–O vibrational modes

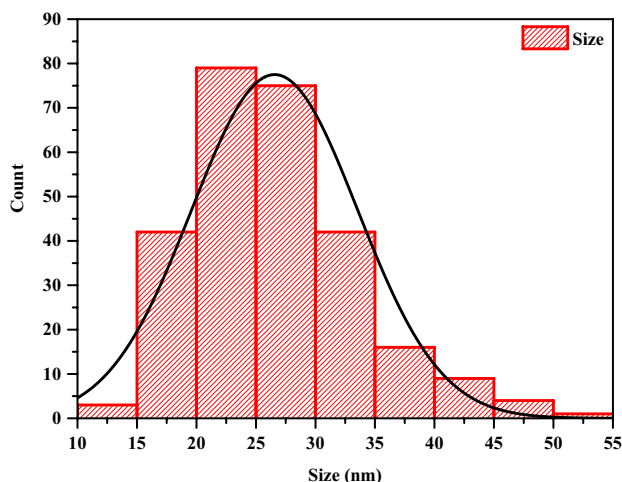
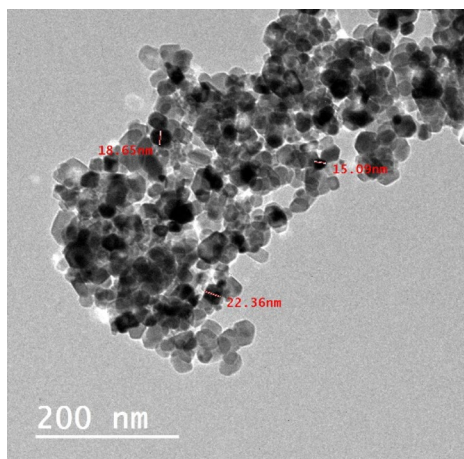


**Fig. 2** a TEM image and b a histogram distribution plot for NiO NPs.

**Table 1** Bands assignment for the FTIR spectra of the synthesized samples

Wavenumber (cm <sup>-1</sup> )	Bands assignment	Sources	References
3307	OH stretching	PVA + CMC + PEDOT:PSS	[17], [4], [20]
2940	CH <sub>2</sub> asymmetric stretching	PVA + CMC	[17, 20], [4]
2907	CH <sub>2</sub> symmetrical stretching	PVA	[18]
1721	C=O stretching	PVA	[20]
1656	RC=C stretching	PVA + PEDOT:PSS	[19], [20]
1603	Asymmetric COO stretching	CMC	[17]
1419	CH <sub>2</sub> scissoring	CMC	[16, 17]
1373	CH <sub>2</sub> bending	PVA	[18]
1321	OH bending	CMC + PVA	[17], [18]
1256	CH <sub>2</sub> bending	PVA	[16]
1086	CO stretching	PVA	[17]
836	CH <sub>2</sub> bending	PVA	[19]
420	Ni–O vibration	NiO NPs	[21]

[21], appeared at 420 cm<sup>-1</sup> after filling and increased with increasing NiO NPs concentration. These results confirmed the interaction of the mixed CMC/PVA/PEDOT:PSS composite with the NiO NPs. The effect of NiO NPs on some characteristic FTIR bands can be used to determine how the filling changed the structural composition of the interpolymer matrix. It should also be noted that the double bond segments in the current structure are considered favorable sites for polarons and/or bipolarons, which could serve as charge carriers hopping sites [22].

### 3.3 UV-visible Absorbance

Figure 4 shows the UV/Vis. absorption of pure NiO NPs, pure CMC/PVA/PEDOT:PSS composite, and the CMC/PVA/PEDOT:PSS composite filled with different concentrations of NiO NPs. Pure NiO NPs showed a sharp peak at 240 nm and a broad peak in the visible region (inset Fig. 4). The pure mixture shows a sharp peak around 228 which can be assigned to the  $\pi \rightarrow \pi^*$  transition [23] due to the presence of C=C and/or C=O in the structure of the blend [24]. The prepared nanocomposites show new peaks at 292 and 422 nm, which gradually increase with increasing NiO NPs content. The appearance of such peaks and their displacement after filling are related to the interaction and complexation between the NiO NPs and the polymeric mixture, which could affect the optical band gaps of the composites.

The optical band gap for the CMC/PVA/PEDOT:PSS and CMC/PVA/PEDOT:PSS/NiO nanocomposite samples can be calculated via Tuac's Eqs. [25–27].

$$\alpha = \frac{A(h\nu - E_g)^r}{h\nu} \quad (1)$$

Where  $E_g$  is the optical energy gap value between the conduction and valence bands,  $\alpha$  is the absorption coefficient,  $A$  is a constant based on the probability of an electronic transition,  $h\nu$  is the incident photon energy, and the power  $r$  defines the type of transition process that occurs in the  $k$ -space.

By plotting the relation between the  $(\alpha h\nu)^{1/2}$  as a function of photon energy (Fig. 5), the optical indirect band gap energy values [25, 28] were derived and listed in Table 2. After filling with NiO NPs, the calculated optical band gap for the pure blend, which was 4.88 eV, was found to be lowered. This effect can be attributed to NiO NPs' capability to modify the electronic structure by producing varying polaronic and defect levels that rise with the density of

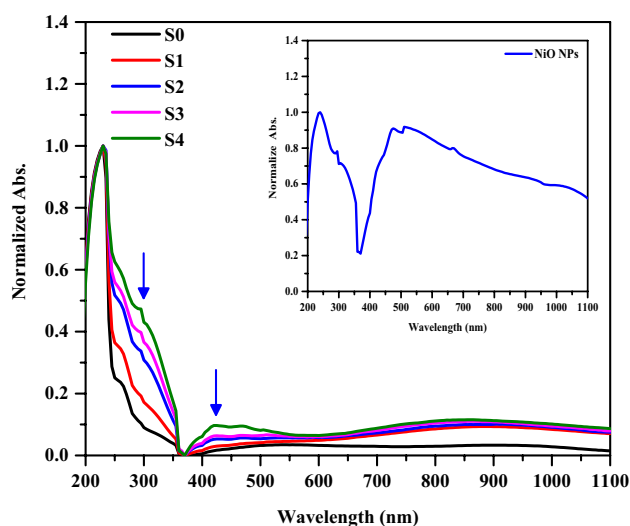


**Fig. 4** UV-vis absorption spectra of PVA/CMC/PEDOT:PSS with various weights of NiO NPs, and inset UV-vis absorption spectrum of NiO NPs.

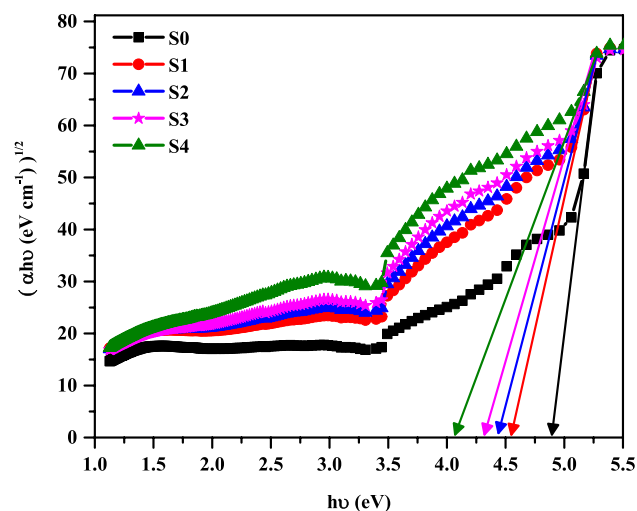


**Fig. 5**  $(\alpha h\nu)^{1/2}$  versus  $h\nu$  of PVA/CMC/PEDOT:PSS with varying contents of NiO NPs.

**Table 2** The indirect energy bandgap for PVA/CMC/PEDOT:PSS with varying contents of NiO NPs.

Films	$E_g$ (eV)
S0	4.88
S1	4.54
S2	4.43
S3	4.31
S4	4.06

localized states  $N(E)$  [29, 30]. This increase in localized states may also reflect the decrease in the crystallinity degree in the filled samples [24].

### 3.4 Conductivity Analysis

A key physical property of polymeric materials is their AC conductivity and dielectric constant, which facilitates the use of synthetic polymers in electrical applications such as contact switches and transistors. The AC conductivity  $\sigma_{ac}$  of the nanocomposite samples is calculated using the following relation [31, 32]:

$$\sigma_{ac} = 2\pi f \epsilon' \epsilon_o \tan\delta \quad (2)$$

where  $\tan\delta$  is the dissipation factor,  $f$  is the applied signal frequency,  $\epsilon_o$  and  $\epsilon'$  are the free-space and material dielectric constants.

Figure 6 shows the AC conductivity of CMC/PVA/PEDOT:PSS composite filled with varied concentrations of NiO NPs as a function of frequency at room temperature. As shown in the figure the conductivity increases gradually with increasing the NiO NPs content, where the distributed NiO NPs in the blend matrix has increased the

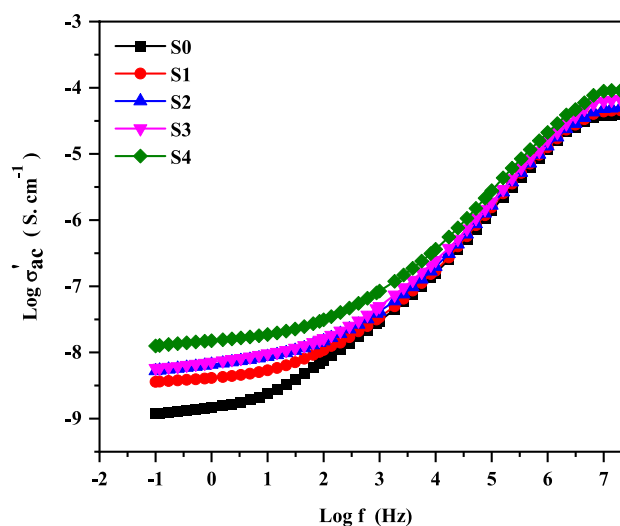


**Fig. 6** AC conductivity of the prepared samples as a function of frequency at room temperature

number of conductive pathways. The conductivity of such composites is known to be influenced by the dispersion, size, shape, and type of the filler components [33–35]. By decreasing the energy barrier and allowing ion mobility, the polymer composite's improved amorphousness may also be responsible for the conductivity enhancement [36].

The figure also shows how frequency-dependent electrical conductivity increased for all samples. The conductivity at the low-frequency region is nearly constant, whereas the high-frequency range exhibits frequency dependence and conforms to the Jonscher power law [20, 36]:

$$\sigma_{ac}(\omega) = \sigma_{dc} + A\omega^s \quad (3)$$

where  $s$  is a temperature and frequency-dependent exponent with a value of  $0 \leq s \leq 1$ ,  $\omega = 2\pi f$  is the angular frequency,  $\sigma_{dc}$  is the DC conductivity (i.e., frequency independent at  $\omega \cong 0$ ), and  $A$  is a temperature-dependent component that influences the degree of polarizability. This is a normal way for many materials to respond, according to Jonscher, and is known as the “universal dynamic response” (UDR) [36]. That the bulk conductivity of the samples, which occurs from charge carriers being shifted, is linked to the low-frequency range and is coupled with the DC conductivity  $\sigma_{dc}$  [33]. In the high applied field frequency range, charge carriers travel more freely than at low frequencies, and so their conductivity increases linearly with the frequency [37]. Furthermore, the loss factor predominates at higher frequencies, leading to a rise in conductivity up to comparably greater values for higher frequency ranges [38]. A lot of polymeric nanocomposites have shown a similar tendency [36, 39].

### 3.5 Impedance Studies ( $Z^*$ )

Impedance spectroscopy is a very efficient and widely used technique to study the electrical properties of electrolytes and their interface with electrically conductive electrodes. The structure of the impedance spectrum provides information about the electrodes' polarization and the type of charge carriers [40]. The complex impedance of the studied films can be analyzed from [41, 42]:

$$Z^* = Z' - iZ'' = \frac{1}{i\omega\epsilon_0\epsilon^*} \quad (4)$$

where  $Z'$  and  $Z''$  are the complex impedance real part and imaginary parts.

Figure 7 shows the Nyquist plots ( $Z''$  vs.  $Z'$ ) for the analyzed system as well as the related equivalent circuit. It has been revealed that the Nyquist curves consist of an angled spike at low frequency and a depressed semi-circular arc at high frequency. The angled spike and semicircle together show the usual behavior of ionic conducting materials [43]. The angled spike indicates that low-frequency ion movement caused the formation of a double-layer capacitance at the electrode/electrolyte interface. The semicircle represents the parallel combination of bulk capacitance caused by the immobile polymer chains and bulk resistance caused by ions' movement. The depressed semicircle appearance indicates a non-Debye type of ion relaxation process. This discrepancy is due to the fact that the potential wells at each site where ion transport occurs are not equal [44]. As the NiO NPs content increase, the semicircle diameter decreases which implies that the bulk resistance decrease.

To illustrate the correlation between electrical properties and microstructure, impedance data is commonly expressed as an equivalent circuit composed of capacitance and resistance. Using EIS software, the acquired impedance data were fitted with an equivalent circuit. This circuit is made up of

a parallel combination of fractal capacity CPE1 and bulk resistance  $R_b$  in series with fractal capacity CPE2, as can be seen in Fig. 7b. CPE is a constant phase element with impedance calculated from [33, 45]:

$$Z_{CPE} = 1/Q(i\omega)^n \quad (5)$$

where  $Q$  stands for the  $1/|Z|$  numerical value at  $\omega = 1$  rad/s, and  $n$  is the element phase, which determines how far the capacitor deviates from being pure. The CPE performs as a pure capacitor when  $n = 1$  and as a pure resistor when  $n = 0$ .

The curves in Fig. 7a were fitted, and the parameters for the equivalent circuit model were derived. Table 3 lists these values. The bulk capacitance values ( $Q_1$ ) in this table have values in the  $10^{-10}$  F range. Furthermore, it was demonstrated that the bulk resistance  $R_b$  decreased with increasing NiO NPs content. The extremely strong concordance between the data and the results of the modeling demonstrates the convenience of the chosen equivalent circuit.

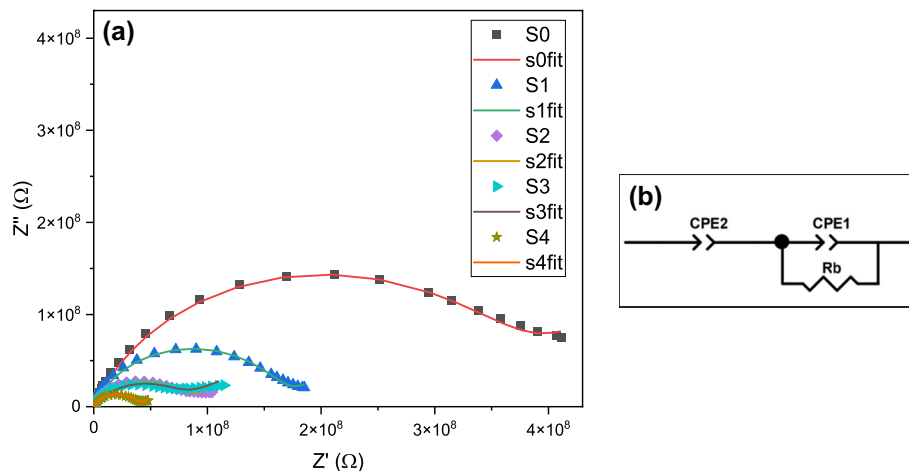
### 3.6 Dielectric Analysis

Dielectric constant  $\epsilon'$  (energy storage) and the dielectric loss  $\epsilon''$  (energy loss) were made between the ranges of  $10^{-1}$  and  $10^7$  Hz at room temperature. Figure 8a and b show log-log

**Table 3** Equivalent circuit fitting parameters

Sample	Fitting parameters				
	$R_b$ ( $\Omega$ )	$Q_1$ (F)	$n_1$	$Q_2$ (F)	$n_2$
S0	$3.62 \times 10^8$	$2.86 \times 10^{-10}$	0.80	$1.54 \times 10^{-8}$	0.50
S1	$1.62 \times 10^8$	$2.68 \times 10^{-10}$	0.81	$3.95 \times 10^{-8}$	0.43
S2	$7.78 \times 10^7$	$4.39 \times 10^{-10}$	0.73	$3.93 \times 10^{-8}$	0.39
S3	$6.78 \times 10^7$	$5.32 \times 10^{-10}$	0.69	$2.35 \times 10^{-8}$	0.35
S4	$3.64 \times 10^7$	$6.18 \times 10^{-10}$	0.76	$9.17 \times 10^{-8}$	0.36

**Fig. 7** a Nyquist plots of the prepared nanocomposite samples, b related equivalent circuit elements



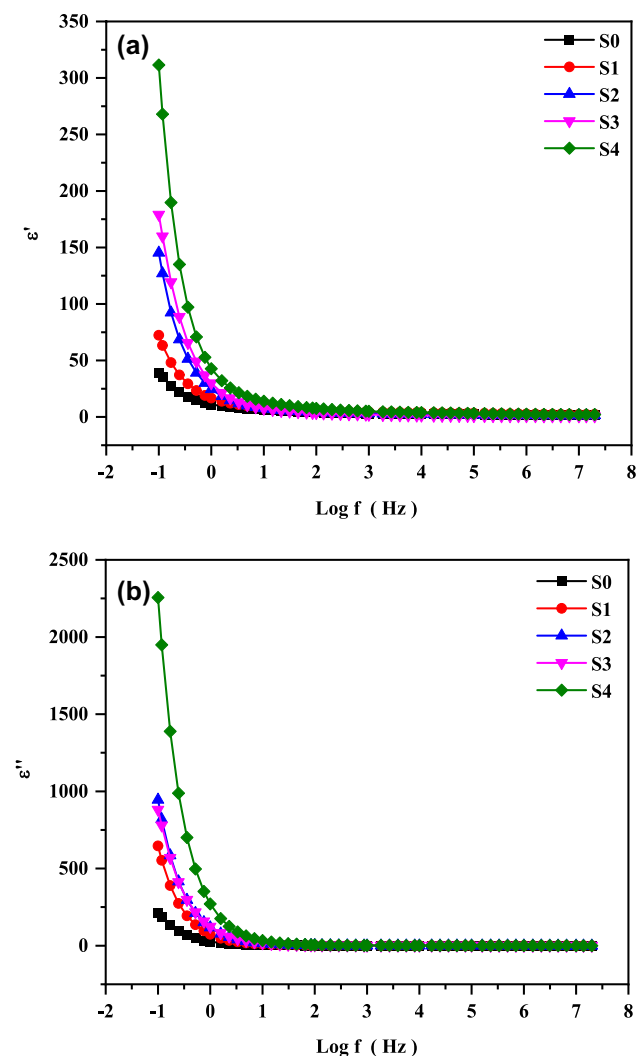


**Fig. 8** The change of **a** dielectric constant  $\epsilon'$  and **b** dielectric loss  $\epsilon''$  versus  $\log$  (F) for the fabricated films

graphs of  $\epsilon'$  and  $\epsilon''$  versus  $\log f$  for the pure CMC/PVA/PEDOT:PSS composite and loaded with various concentrations of NiO NPs. The figures show that  $\epsilon'$  and  $\epsilon''$  have large values at low frequencies and that their values drop with increasing frequency for all samples. At high frequencies,  $\epsilon'$  and  $\epsilon''$  become extremely small and exhibit behavior that is almost frequency independent.

The interfacial effects present in the majority of the sample and the electrode effects might both be responsible for the high values of  $\epsilon'$  and  $\epsilon''$ . Additionally, it is known that for polar materials, the initial value of  $\epsilon'$  and  $\epsilon''$  is large, but as the frequency of the field increases, the value starts to decline because the dipoles cannot keep up with the field changes [46]. The periodic reversal of the electric field at high frequencies happens so quickly that there is no extra ion diffusion in the field's direction. The value of  $\epsilon'$  and  $\epsilon''$  diminishes as the polarization brought on by the charge

buildup does [20, 47]. The decrease in  $\epsilon''$  with frequency is also related to the presence of high dislocation density in the sample because the presence of defects/dislocations in the sample reduces the motion of charge carriers across the sample [48].

It can be observed that for all frequency ranges, the values of  $\epsilon'$  and  $\epsilon''$  for the filled films are greater than those for pure CMC/PVA/PEDOT:PSS composite and rise with increasing filling content. Due to the polarization of the polymer/filler interfaces, the rise in  $\epsilon'$  and  $\epsilon''$  with increased NiO NPs concentration may be explained by an increase in the accumulated charge. The charge quantity receives an additional boost from polarization. Therefore, the dielectric constant of the NiO NPs-filled polymer will be greater than the dielectric constant of the pure blend.

## 4 Conclusion

The solution casting approach was used to fabricate nanocomposite films comprised of a CMC/PVA/PEDOT:PSS composite filled with various concentrations of NiO NPs. According to XRD analyses of the filled samples, the crystallinity of the NiO NPs increased at the expense of the CMC/PVA/PEDOT:PSS composite films after filling. The semi-crystalline nature of the examined nanocomposite films was also demonstrated. FTIR, XRD, and UV/visible analysis revealed the complexity and intermolecular interaction between the pure blend and NiO NPs. The assigned double bond in the FTIR spectra indicated the presence of polarons and/or bipolarons in the polymer matrix, which could serve as charge carriers hopping sites. The UV and visible spectra analysis revealed that when the NiO NPs concentration rose, the optical energy gaps for the indirectly allowed transitions shrank. Impedance spectroscopy at room temperature revealed that the nanocomposite films filled with NiO NPs improve AC electrical conductivity, dielectric constant, and dielectric loss. Finding the corresponding electrical circuit for the samples was made possible by the analysis of impedance components  $Z'$  and  $Z''$ . These nanocomposite films may compete for use in optoelectronic applications as a result of their improvement in optical and electrical properties.

**Author Contributions** ES planned and performed the experiments and wrote the manuscript. AET wrote and revised the manuscript.

**Funding** Open access funding provided by The Science, Technology & Innovation Funding Authority (STDF) in cooperation with The Egyptian Knowledge Bank (EKB). The authors have not disclosed any funding.

**Data Availability** All data produced during this work are included in this published article.

## Declarations

**Conflict of interest** The authors declare that they have no competing interest.

**Open Access** This article is licensed under a Creative Commons Attribution 4.0 International License, which permits use, sharing, adaptation, distribution and reproduction in any medium or format, as long as you give appropriate credit to the original author(s) and the source, provide a link to the Creative Commons licence, and indicate if changes were made. The images or other third party material in this article are included in the article's Creative Commons licence, unless indicated otherwise in a credit line to the material. If material is not included in the article's Creative Commons licence and your intended use is not permitted by statutory regulation or exceeds the permitted use, you will need to obtain permission directly from the copyright holder. To view a copy of this licence, visit <http://creativecommons.org/licenses/by/4.0/>.

## References

- E. Salim, *J. Mater. Sci.: Mater. Electron* **32**, 28830 (2021)
- A.M. el Sayed, S. El-Gamal, *J. Polym. Res* **22**, 97 (2015)
- E.M. Abdallah, M.A. Morsi, G.M. Asnag, A.E. Tarabiah, *Int. J. Energy Res.* **46**, 10741 (2022)
- A.E. Tarabiah, H.A. Alhadlaq, Z.M. Alaizeri, A.A.A. Ahmed, G.M. Asnag, M. Ahamed, *J. Polym. Res* **29**, 167 (2022)
- S. Md, Md.S. Rahman, A.S. Hasan, S. Nitai, A.K. Nam, Md.S. Karmakar, M.J.A. Ahsan, Shiddiky, M.B. Ahmed, *Polym. (Basel)* **13**, 1345 (2021)
- G. Sahu, J. Tripathy, B.P. Sahoo, *Polym. Compos.* **41**, 4411 (2020)
- K. Rajesh, V. Crasta, N.B. Rithin Kumar, G. Shetty, P.D. Rekha, *J. Polym. Res* **26**, 99 (2019)
- C. Chen, A. Kine, R.D. Nelson, J.C. LaRue, *Synth. Met.* **206**, 106 (2015)
- N. SRIVASTAVA and P.C. SRIVASTAVA, *Bull. Mater. Sci* **33**, 653 (2010)
- M. Shkir, K.v. Chandekar, A. Khan, T. Alshahrani, A. Mohamed El-Toni, M.A. Sayed, A.K. Singh, A.A. Ansari, M.R. Muthumareeswaran, A. Aldalbahi, R.K. Gupta, S. AlFaify, *Mater. Sci. Semicond. Process.* **126**, 105647 (2021)
- H. Ahmad, S.A. Reduan, N. Yusoff, *RSC Adv.* **8**, 25592 (2018)
- A. Magdy, A. El-Shaer, A.H. EL-Farrash, E. Salim, *Sci. Rep.* **12**, 21489 (2022)
- T.S. Soliman, S.A. Vshivkov, S.I. Elkalashy, *Polym. Compos.* **41**, 3340 (2020)
- T.S. Soliman, S.A. Vshivkov, *J. Non Cryst. Solids* **519**, 119452 (2019)
- M.A. Hamdan, N.A. Ramli, N.A. Othman, K.N. Mohd Amin, F. Adam, *Mater. Today Proc* **42**, 56 (2021)
- M.A. Morsi, A.H. Oraby, A.G. Elshahawy, R.M. Abd El-Hady, *J. Mater. Res. Technol* **8**, 5996 (2019)
- A.A. Al-Muntaser, R.A. Pashameah, K. Sharma, E. Alzahrani, A.E. Tarabiah, *Int. J. Energy Res.* **46**, 23984 (2022)
- A.L. Waly, A.M. Abdelghany, A.E. Tarabiah, *J. Mater. Sci.: Mater. Electron* **33**, 23174 (2022)
- A.L. Waly, A.M. Abdelghany, A.E. Tarabiah, *J. Mater. Res. Technol.* **14**, 2962 (2021)
- E. Salim, W. Hany, A.G. Elshahawy, A.H. Oraby, *Sci. Rep.* **12**, 21201 (2022)
- A. Sani, D. Hassan, A.T. Khalil, A. Mughal, A. El-Mallul, M. Ayaz, Z. Yessimbekov, Z.K. Shinwari, M. Maaza, *J. Biomol. Struct. Dyn.* **39**, 4133 (2021)
- A. Tawansi, H.M. Zidan, Y.M. Moustafa, A.H. Eldumiaty, *Phys. Scr.* **55**, 243 (1997)
- M.R. Atta, Q.A. Alsulami, G.M. Asnag, A. Rajeh, *J. Mater. Sci.: Mater. Electron* **32**, 10443 (2021)
- E.M. Abdallah, T.F. Qahtan, E.M. Abdelrazek, G.M. Asnag, M.A. Morsi, *Opt. Mater. (Amst)* **134**, 113092 (2022)
- A.M. Alshehari, E. Salim, A.H. Oraby, *J. Mater. Res. Technol.* **15**, 5615 (2021)
- K.v. Chandekar, F.H. Alkallas, A.B.G. Trabelsi, M. Shkir, J. Hakami, A. Khan, H.E. Ali, N.S. Awwad, S. AlFaify, *Phys. B Condens Matter* **641**, 414099 (2022)
- A.B.G. Trabelsi, K.V. Chandekar, F.H. Alkallas, I.M. Ashraf, J. Hakami, M. Shkir, A. Kaushik, S. AlFaify, *J. Mater. Res. Technol.* **21**, 3982 (2022)
- M.A. Gaffar, A.A. El-Fadl, S.B. Anooz, *Phys. B Condens Matter* **327**, 43 (2003)
- I.S. Elashmawi, A.A. Al-Muntaser, A.M. Ismail, *Opt. Mater. (Amst)* **126**, 112220 (2022)
- R. Murri, L. Schiavulli, N. Pinto, T. Ligonzo, *J. Non Cryst. Solids* **139**, 60 (1992)
- K.v. Chandekar, M. Shkir, A. Khan, M.A. Sayed, N. Alotaibi, T. Alshahrani, H. Algarni, S. AlFaify, *J. Mater. Res. Technol.* **15**, 2584 (2021)
- K.v. Mohd. Shkir, T. Chandekar, A. Alshahrani, A. Kumar, Khan, S. AlFaify, *Eur. Phys. J. Plus* **135**, 816 (2020)
- M. Rahaman, A. Aldalbahi, P. Govindasami, N. Khanam, S. Bhandari, P. Feng, T. Altalhi, *Polym. (Basel)* **9**, 527 (2017)
- N. Singh, A. Qureshi, A. Rakshit, D. Avasthi, *Bull. Mater. Sci* **29**, 605 (2006)
- K.v. Chandekar, M. Shkir, B. Palanivel, Z. Ahmad, H. Algarni, S. AlFaify, *Solid State Sci* **122**, 106773 (2021)
- E.M. Abdelrazek, A.M. Abdelghany, A.E. Tarabiah, H.M. Zidan, *J. Mater. Sci.: Mater. Electron* **30**, 15521 (2019)
- K.S. Hemalatha, G. Sriprakash, M.V.N. Ambika Prasad, R. Damle, K. Rukmani, *J. Appl. Phys.* **118**, 154103 (2015)
- M. Jebli, J. Ch Rayssi, M. Dhahri, M. ben Henda, H. Belmabrouk, A. Bajahzar, *RSC Adv* **11**, 23664 (2021)
- M. Yang, H. Zhao, C. Hu, P. Haghi-Ashtiani, D. He, Z.-M. Dang, J. Bai, *Phys. Chem. Chem. Phys.* **20**, 2777 (2018)
- D.C. Sinclair, A.R. West, *J. Appl. Phys.* **66**, 3850 (1989)
- R. Khalil, *Appl. Phys. A* **123**, 422 (2017)
- K.v. Chandekar, M. Shkir, A. Khan, S. AlFaify, *Mater. Sci. Semicond. Process.* **118**, 105184 (2020)
- M. Prabu, S. Selvasekarapandian, A.R. Kulkarni, G. Hirankumar, A. Sakunthala, *Ionics (Kiel)* **16**, 317 (2010)
- S. Lanfredi, *Solid State Ion* **146**, 329 (2002)
- A.B.G. Trabelsi, F.H. Alkallas, K.v. Chandekar, A. Kumar, M. Ubaidullah, M. Shkir, A. Khan, M. Aslam, Manthrammel, S. AlFaify, *Mater. Chem. Phys.* **297**, 127299 (2023)
- M. Shkir, A. Khan, K. v. Chandekar, M.A. Sayed, A.M. El-Toni, A.A. Ansari, S.F. Adil, H. Ghaithan, H. Algarni, S. AlFaify, *Ceram. Int.* **47**, 15611 (2021)
- H.M. Zidan, *Int. J. Electrochem. Sci.* **11**, 9041 (2016)
- K.v. Chandekar, M. Shkir, S.P. Yadav, P.K. Behera, S. AlFaify, *J. Mater. Sci.: Mater. Electron* **33**, 3849 (2022)

**Publisher's Note** Springer Nature remains neutral with regard to jurisdictional claims in published maps and institutional affiliations.